Anisotropy of <a > slip behaviour in single-colony lamellar structures of Ti–6Al–4V

Htwe, Yin; Kwak, Kwangsik; Kishi, Daichi; Mine, Yoji; Ding, Rengen; Bowen, Paul; Takashima, Kazuki

DOI:
10.1016/j.msea.2018.01.013

Author’s Accepted Manuscript

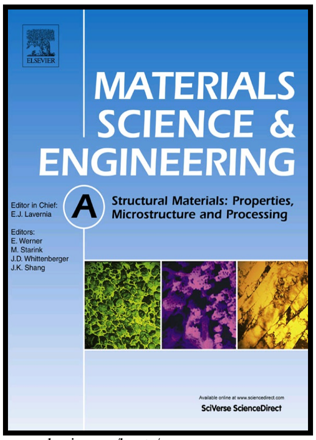

www.elsevier.com/locate/msea

Anisotropy of <*a*> slip beh*a*viour in single-colony lamellar structures of Ti–6Al–4V

Yin Htwe, Kwangsik Kwak, Daichi Kishi, Yoji Mine, Rengen Ding, Paul Bowen, Kazuki Takashima

PII: S0921-5093(18)30009-1
DOI: https://doi.org/10.1016/j.msea.2018.01.013
Reference: MSA35967

To appear in: *Materials Science & Engineering A*

Received date: 8 August 2017
Revised date: 13 November 2017
Accepted date: 3 January 2018

Cite this article as: Yin Htwe, Kwangsik Kwak, Daichi Kishi, Yoji Mine, Rengen Ding, Paul Bowen and Kazuki Takashima, Anisotropy of <*a*> slip beh*a*viour in single-colony lamellar structures of Ti–6Al–4V, *Materials Science & Engineering A,* https://doi.org/10.1016/j.msea.2018.01.013

Anisotropy of <*a*> slip behaviour in single-colony lamellar structures of Ti–6Al–4V

Yin Htwe[a], Kwangsik Kwak[a], Daichi Kishi[a], Yoji Mine[a,*], Rengen Ding[b], Paul Bowen[b] and Kazuki Takashima[a]

[a] Department of Materials Science and Engineering, Kumamoto University, Kurokami, Chuo-ku, Kumamoto 860-8555, Japan

[b] School of Metallurgy and Materials, University of Birmingham, Edgbaston, Birmingham B15 2TT, United Kingdom

[*] Corresponding author. E-mail address: mine@msre.kumamoto-u.ac.jp

Abstract

Micro-tensile tests on single-colony specimens of Ti–6Al–4V alloy with a fine lamellar microstructure revealed that the critical resolved shear stress of the basal slip was lower than that of the prismatic slip. This has been attributed to easier slip transmission within the habit plane at the α/β boundaries.

***Keywords**:* titanium alloys; plasticity; grains and interfaces

1. Introduction

Additive manufacturing (AM) processes of metallic materials that control the microstructure and shape of three-dimensional structures simultaneously have attracted much attention for application in aerospace components and biomedical devices. Ti–6Al–4V alloy, which is a hexagonal close packed (hcp) α and body-centred cubic (bcc) β two-phase alloy, is a candidate used for metal-based AM processes. For AM Ti–6Al–4V, β crystals grow preferentially along the <001> direction during solidification [1,2]. Moreover, below the β transus, an α or α' martensite phase is transformed from the β phase according to the Burgers orientation relationship (OR): $(0001)_{\alpha}//(110)_{\beta}$ and $[2\bar{1}\bar{1}0]_{\alpha}//[1\bar{1}\bar{1}]_{\beta}$ [3]. Therefore, AM Ti–6Al–4V alloy tends to form a strong texture, leading to anisotropic mechanical properties [4–6]. Although AM Ti–6Al–4V often suffers a trade-off between strength and ductility [6,7], post-AM thermal processing results in high strength and moderate ductility through the formation of fine lamellar microstructures [8,9]. For the lamellar microstructure, the yield stress increases with the decrease in lath spacing based on the Hall–Petch relationship [10], whereas the deformation behaviour depends not only on the strong anisotropy of plasticity in the hcp structure but also the slip transmission at α/β interphase boundary.

Tensile and compression tests using near-α alloys of Ti–5Al–2.5Sn–0.5Fe and Ti–

6Al–2Sn–4Zr–2Mo–0.1Si [11–13] reveal a strong anisotropy in the <*a*> slip behaviour on the prismatic and basal planes in the α phase. The critical resolved shear stress (CRSS) of the prismatic slip with the $[2\bar{1}\bar{1}0]$: *a*1 slip direction, which is nearly parallel to $[\bar{1}\bar{1}1]$: *b*1 on $(1\bar{1}2)$ in the β phase, is lower than that of the other $[\bar{1}2\bar{1}0]$: *a*2 prismatic slip and $[\bar{1}\bar{1}20]$: *a*3 prismatic slip, which are both away from $<111>_{\beta}$ [12,13]. With regard to basal slip behaviour, the influence of the CRSS appears different for tensile and compression testing [13]. A tensile test revealed that the CRSS of the *a*3 basal slip is lower than of both *a*1 and *a*2 basal slip, but the authors could not explain this anisotropy by considering the Burgers OR [12,13]. Recently, a micro-compression study by Jun et al. on the Ti–6Al–2Sn–4Zr–2Mo alloy suggested that α/β morphology can influence local deformation behaviour significantly [14].

With regard to the Ti–6Al–4V alloy of interest here, Ambard et al. observed [15] that the main deformation system in globular grains is prismatic slip, whereas in lamellar colonies, basal slip is activated. Micro-cantilever specimens with single colony structures were used under a bending moment to clarify a second-phase strengthening effect [16] and the anisotropy of the <*c*+*a*> slip behaviour [17,18]. However, anisotropy of <*a*> slip behaviour has not yet been clarified. It is difficult to analyse the deformation behaviour using micro-bending tests owing to their complicated stress conditions. In contrast, micro-tensile tests have been used to elucidate the plastic behaviour of hierarchical microstructures such as a lath martensitic steel [19,20]. This current study uses micro-tensile tests with single colony specimens to understand the anisotropy of the <*a*> slip behaviour of a Ti–6Al–4V alloy with a fine lamellar microstructure.

2. Material and methods

The material used in this study was a hot-rolled Ti–6Al–4V (mass%) alloy. The actual composition measured by electron probe micro analyser was Ti–6.1Al–4.6V–0.1Fe. The hot-rolled plate was heated to 1323 K within the β region and was maintained for 900 s followed by air cooling to 993 K. Subsequently, maintaining this temperature for 7.2 ks led to the formation of a lamellar microstructure with an average prior β grain size of approximately 220 μm. Small samples were cut and thinned to less than 25 μm by grinding with emery paper. Both surfaces of the samples were electrochemically polished. The crystallographic orientation of the α phase was determined using a scanning electron microscope equipped with an electron back-scatter diffraction (EBSD) detector and orientation imaging microscopy software TSL OIM v.7.1.0. Micro-tensile specimens with gauge section dimensions of approximately 20 × 20 × 50 μm were fabricated from grains with their foil planes parallel to $(0001)_\alpha$ and $\{10\bar{1}0\}_\alpha$ using a focused ion beam (FIB). The gauge section was included within a single colony of the lamellar microstructure. The loading directions were aligned at an angle of approximately 45° with respect to the <*a*> directions on the prismatic and basal planes in the α phase, i.e. the prismatic and basal slips, respectively, were expected to be primarily activated, as shown in Fig. 1. Tensile tests were performed at room temperature in laboratory air at atmospheric pressure and the displacement rate was set to 0.1 μm s^{-1}. This corresponds to an initial strain rate of 2×10^{-3} s^{-1}. After tensile testing, some samples were fabricated using FIB milling. Transmission electron microscopy (TEM) examination was performed using a JEOL JEM-2100PLUS microscope operating at an accelerating voltage of 200 kV.

3. Results and discussion

Figure 2 shows the TEM bright-field image and selected area electron diffraction (SAED) pattern of a typical lamellar microstructure in this study. The average lamellar spacing and β lath thickness were measured to be approximately 0.73 and 0.10 μm, respectively, and the β phase fraction was approximately 13%. The crystallographic orientation of the α and β phases was confirmed to be the Burgers OR: $(0001)_\alpha//(110)_\beta$ and $[2\bar{1}\bar{1}0]_\alpha//[1\bar{1}\bar{1}]_\beta$, as illustrated in Figs. 2b and c, i.e. the $[2\bar{1}\bar{1}0]_\alpha$: *a*1 direction was nearly parallel to the $[1\bar{1}\bar{1}]_\beta$: *b*1 direction, the misorientation angle between $[\bar{1}2\bar{1}0]_\alpha$: *a*2 and $[\bar{1}1\bar{1}]_\beta$: *b*2 was approximately 11°, and $[\bar{1}\bar{1}20]_\alpha$: *a*3 had no nearly parallel $\langle 1\bar{1}\bar{1}\rangle_\beta$

direction, but was inclined at an angle of approximately 5° with respect to $[001]_\beta$. Further, the misorientation was approximately 9° between the $(0\bar{1}10)_\alpha$ prismatic plane and the broad face of the lamellae.

Figures 3a and b show the nominal stress–strain curves (nominal stresses are based on the load divided by the original cross-sectional area) obtained for the prismatic slip (Pr) and basal slip (Ba) specimens, respectively. In Pr specimens, yielding by prismatic slip exhibiting the highest Schmid factor was followed by slight strain-hardening towards the maximum nominal tensile stress applied of 790–930 MPa, and subsequently the flow stress gradually decreased with an increase in strain, resulting in a fracture strain of 24–40%. In contrast, the Ba specimens exhibited a linear relationship between stress and strain until the stress almost reached the maximum nominal tensile stress applied of 700–750 MPa. Notably, a long plateau regime appeared in the Ba specimens through strain softening, followed by moderate strain hardening. The Ba specimens exhibited a large fracture strain of 80–100% but a lower proof stress compared with the Pr specimens.

Table 1 presents the tensile properties and the CRSS, which is defined as the resolved shear stress for yielding at a plastic strain of 0.2%. The lamellar colony is considered to behave as a single crystal because the α and β phases have a defined crystallographic

OR, i.e. the Burgers OR. When comparing the Ba and Pr specimens, it was observed that the CRSS of the basal slip (341–366 MPa) was lower than that of the prismatic slip (376–453 MPa). A compression test study by Williams et al. [21] on the Ti–Al solid-solution single crystals revealed that, in a Ti–6.6% Al alloy, the CRSS of the basal slip is nearly equivalent to that of the prismatic slip, whereas prismatic slip is the primary slip system in pure titanium. Figure 4 shows schematic illustrations indicating the difference in slip blocking by β laths. When prismatic slip is primarily activated in the α phase, dislocation motion is hindered by pile-up dislocations at α/β interphase-boundaries (Fig. 4a). With respect to Ba specimens, it is deduced that a segment of the slip line is retarded in the β phase (Fig. 4b). Therefore, inhibition of α slip activity by β phase may be smaller for Ba specimens than for Pr specimens.

For the Pr specimens, the CRSS of the *a*1 slip was determined to be 376 MPa, and the CRSS of *a*2 and *a*3 slip was approximately 450 MPa, which is 20% higher than the CRSS of the *a*1 slip. A compression study by Savage et al. [12] on the Ti–6Al–2Sn–4Zr–2Mo–0.1Si single-colony specimens demonstrated that the CRSS of *a*2 and *a*3 prismatic slip was 3 and 11% higher, respectively, than that of the *a*1 prismatic slip, depending on the incompatibility with slip in the β phase based on the Burgers OR. However, these differences in CRSS are somewhat smaller than those in the case of the

Ti–6Al–4V alloy used in the present study. This may perhaps be attributed to the difference in the frequency of slip interaction at the α/β boundaries. Figure 5 shows schematic illustrations of the orientation and distribution of β laths intersecting with the primarily activated slip plane. For Pr–*a*1 specimen, the $(0\bar{1}10)$ slip plane was intersected at a shallow angle of approximately 9° to the broad face of the β phase (Fig. 5a). Only six β laths were included in the area (28×20 μm^2) swept by the *a*1 slip throughout the specimen width (Fig. 5a), whereas the numbers of β laths for the *a*2 and *a*3 specimens were 6 and 5 times higher, respectively, than those in the case of the *a*1 specimen (Figs. 5b and c). With regard to the Ba specimens, the frequency of slip interaction at the α/β boundaries was the same, whereas angles of intersection of β laths differed from each other (Figs. 1d–f). Therefore, it is deduced that the difference in CRSS in Ba specimens reflects the difficulty of slip transmission based on the Burgers OR.

Figure 6 shows optical micrographs captured at a given strain during the plastic deformation process and the inverse pole figure maps along the loading direction after failure in the Pr–*a*1 and Ba–*a*1 specimens. In the Pr-a1 specimen, the specimen width decreased with activation of the *a*1 prismatic slip beyond the first apex in the stress–strain curve (Figs. 6a and b) and subsequently, in the plateau regime of stress–strain behaviour (Fig. 3a), this initial yielding region spread through the gauge length and deformation now occurred symmetrically with respect to the neutral plane along the loading axis (Fig. 6c). Further, fractographic observation demonstrated no shrinkage in the thickness of the Pr specimens. Therefore, crystal rotation owing to the *a*1 prismatic slip activated the *a*2 prismatic slip in turn, as the Schmid factor of the *a*1 slip decreased. This is supported by the EBSD observation of the fracture specimen (Fig. 6d).

For the Ba-*a*1 specimens, local yielding occurred during the strain softening regime (Figs. 6e and f), and this locally yielding region spread uniformly throughout the gauge length (Fig. 6g), corresponding to moderate strain hardening (Fig. 3b). Finally, necking occurred through the specimen thickness (Fig. 6h). The EBSD observation revealed significant crystal rotation from the shoulder of the specimen to the fracture location (regions 1 to 4 in Fig. 6i). Between regions 1 and 2, a boundary was formed with a rotation angle of approximately 18.5° with respect to the $[01\bar{1}0]$ axis. From regions 1 to 3, crystal rotation occurred with the activation of the *a*1 basal slip. In region 3, the *a*1 direction was aligned at an angle of 18.7° with respect to the loading direction. In region 4, the crystal was rotated at approximately 30° with respect to the *c* axis. This indicates that prismatic slip was activated in the region near the fracture surface. Further, crystal rotation owing to the basal slip reduced its own Schmid factor, but increased that for prismatic slip. Therefore, in the Ba-*a*1 specimen, a large uniform elongation was deduced to be attained by activation of the basal slip, such as a Lüders elongation in mild steel, followed by onset of prismatic slip during necking.

4. Conclusions

In summary, the CRSS for basal slip was determined to be 341–367 MPa, which is lower than that for prismatic slip (376–453 MPa) in single-colony lamellar structures of the Ti–6Al–4V alloy. This is attributed to easier slip transmission within the habit plane $(0001)_{\alpha}//(110)_{\beta}$. The difference in CRSS for different <*a*> slip directions was smaller on the basal plane than on the prismatic plane. This is attributed to the difference in the frequency of α/β slip interaction. Elongation of basal slip specimens at fracture was measured to be 80–100%, which is approximately three times higher than that of prismatic slip specimens. Thus <*a*> slip behaviour is deduced to contribute to strengthening without reducing a moderate ductility.

The authors are indebted to Mr. M. Yoshimoto, Dr. M. Tsushida and Dr. T. Yamamuro, Kumamoto University for their assistance in the micro-mechanical tests and TEM studies. This work was supported in part by a Grant-in-Aid for Scientific Research (A) JP15H02302 from the Japan Society for the Promotion of Science (JSPS) and in part by ‘Program for Advancing Strategic International Networks to Accelerate the Circulation of Talented Researchers' R2608.

References

[1] S.S. Al-Bermani, M.L. Blackmore, W. Zhang, I. Todd, The origin of microstructural diversity, texture, and mechanical properties in electron beam melted Ti-6Al-4V, Metall. Mater. Trans. A 41 (2010) 3422–3434.

[2] A.A. Antonysamy, J. Meyer, P.B. Prangnell, Effect of build geometry on the β-grain structure and texture in additive manufacture of Ti–6Al–4V by selective electron beam melting, Mater. Charact. 84 (2013) 153–168.

[3] W.G. Burgers, On the process of transition of the cubic-body-centered modification into the hexagonal-close-packed modification of zirconium, Physica 1 (1934) 561–586.

[4] T. Vilaro, C. Colin, J.D. Bartout, As-fabricated and heat-treated microstructures of the Ti–6Al–4V alloy processed by selective laser melting, Metall. Mater. Trans. A 42 (2011) 3190–3199.

[5] M. Simonelli, Y.Y. Tsea, C. Tuck, Effect of the build orientation on the mechanical properties and fracture modes of SLM Ti–6Al–4V, Mater. Sci. Eng. A 616 (2014) 1–11.

[6] P. Åkerfeldt, M.L. Antti, R. Pederson, Influence of microstructure on mechanical properties of laser metal wire-deposited Ti-6Al-4V, Mater. Sci. Eng. A 674 (2016) 428–437.

[7] L.E. Murr, S.A. Quinones, S.M. Gaytan, M.I. Lopez, A. Rodela, E.Y. Martinez, D.H.

Hernandez, E. Martinez, F. Medina, R.B. Wicker, Microstructure and mechanical behavior of Ti–6Al–4V produced by rapid-layer manufacturing, for biomedical applications, J. Mech. Behav. Biomed. Mater. 2 (2009) 20–32.

[8] W. Xu, M. Brandt, S. Sun, J. Elambasseril, Q. Liu, K. Latham, K. Xia, M. Qian, Additive manufacturing of strong and ductile Ti–6Al–4V by selective laser melting via in situ martensite decomposition, Acta Mater. 85 (2015) 74–84.

[9] M. Qian, W. Xu, M. Brandt, H.P. Tang, Additive manufacturing and postprocessing of Ti–6Al–4V for superior mechanical properties, MRS Bulletin 41 (2016) 775–783.

[10] H. Galarraga, R.J. Warren, D.A. Lados, R.R. Dehoff, M.M. Kirka, P. Nandwana, Effects of heat treatments on microstructure and properties of Ti–6Al–4V ELI alloy fabricated by electron beam melting (EBM), Mater. Sci. Eng. A 685 (2017) 417–428.

[11] S. Suri, G.B. Viswanathan, T. Neeraj, D.-H. Hou, M.J. Mills, Room temperature deformation and mechanisms of slip transmission in oriented single-colony crystals of an α/β titanium alloy, Acta Mater. 47 (1999) 1019–1034.

[12] M.F. Savage, J. Tatalovich, M. Zupan, K.J. Hemker, M.J. Mills, Deformation mechanisms and microtensile behavior of single colony Ti–6242Si, Mater. Sci. Eng. A 319–321 (2001) 398–403.

[13] M.F. Savage, J. Tatalovich, M.J. Mills, Anisotropy in the room-temperature

deformation of α–β colonies in titanium alloys: role of the α–β interface, Phil. Mag. 84 (2004) 1127–1154.

[14] T.S. Jun, G. Sernicola, F.P.E. Dunne, T.B. Britton, Local deformation mechanisms of two-phase Ti alloy, Mater. Sci. Eng. A 649 (2016) 39–47.

[15] A. Ambard, L. Guétaz, F. Louchet, D. Guichard, Role of interphases in the deformation mechanisms of an α/β titanium alloy at 20 K, Mater. Sci. Eng. A 319–321 (2001) 404–408.

[16] J. Gong, A.J. Wilkinson, A microcantilever investigation of size effect, solid-solution strengthening and second-phase strengthening for <a> prism slip in alpha-Ti, Acta Mater 59 (2011) 5970–5981.

[17] R. Ding, J. Gong, A.J. Wilkinson, I.P. Jones, Transmission electron microscopy of deformed Ti–6Al–4 V micro-cantilevers, Phil. Mag. 92 (2012) 3290–3314.

[18] R. Ding, J. Gong, A.J. Wilkinson, I.P. Jones, <c+a> Dislocations in deformed Ti–6Al–4V micro-cantilevers, Acta Mater 76 (2014) 127–134.

[19] Y. Mine, K. Hirashita, H. Takashima, M. Matsuda, K. Takashima, Micro-tension behaviour of lath martensite structures of carbon steel, Mater. Sci. Eng. A 560 (2013) 535–544.

[20] K. Kwak, T. Mayama, Y. Mine, K. Takashima, Anisotropy of strength and plasticity

in lath martensite steel, Mater. Sci. Eng. A 674 (2016) 104–116.

[21] J.C. Williams, R.G. Baggerly, N.E. Paton, Deformation behavior of HCP Ti-Al alloy single crystals, Metall. Mater. Trans. A 33 (2002) 837–850.

Fig. 1 Schematic illustrations of crystallographic orientations of slip planes and directions.

Fig. 2 TEM bright-field micrograph and SAED pattern showing crystallographic orientation relationship between the α and β phases.

Fig. 3 Stress–strain curves for (a) Pr and (b) Ba specimens.

Fig. 4 Schematic illustrations showing different slip blocking morphologies at β laths which intersect with primarily activated slip.

Fig. 5 Schematic illustrations showing orientation and distribution of β laths which intersect with primarily activated slip for Pr specimens.

Fig. 6 Optical microscopy images captured during micro-tensile testing and EBSD map colour-coded along the loading direction after failure in (a–d) Pr–*a*1 and (e–i) Ba–*a*1.

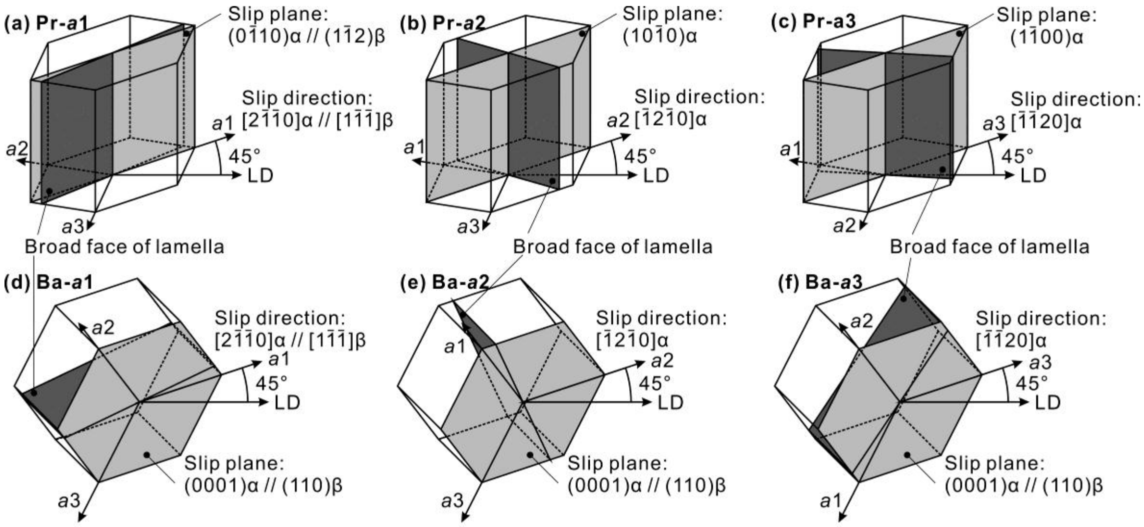

Fig. 1 Schematic illustrations of crystallographic orientations of slip planes and directions.

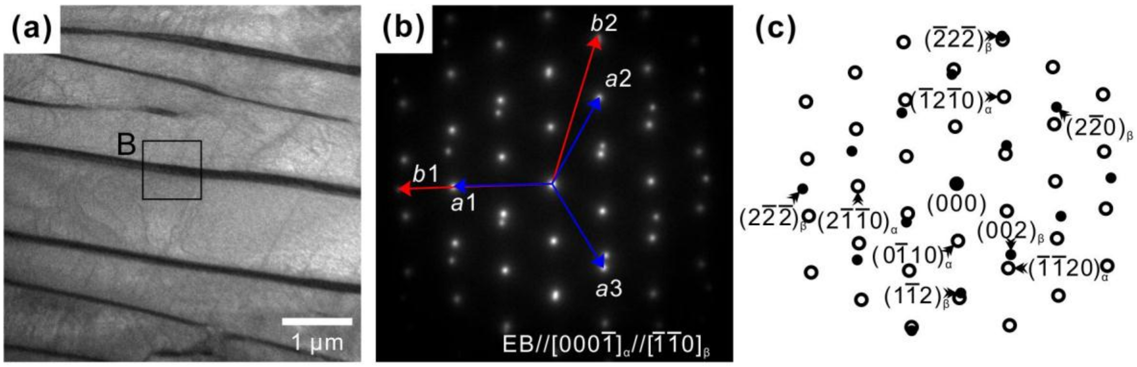

Fig. 2 TEM bright-field micrograph and SAED pattern showing crystallographic orientation relationship between the α and β phases.

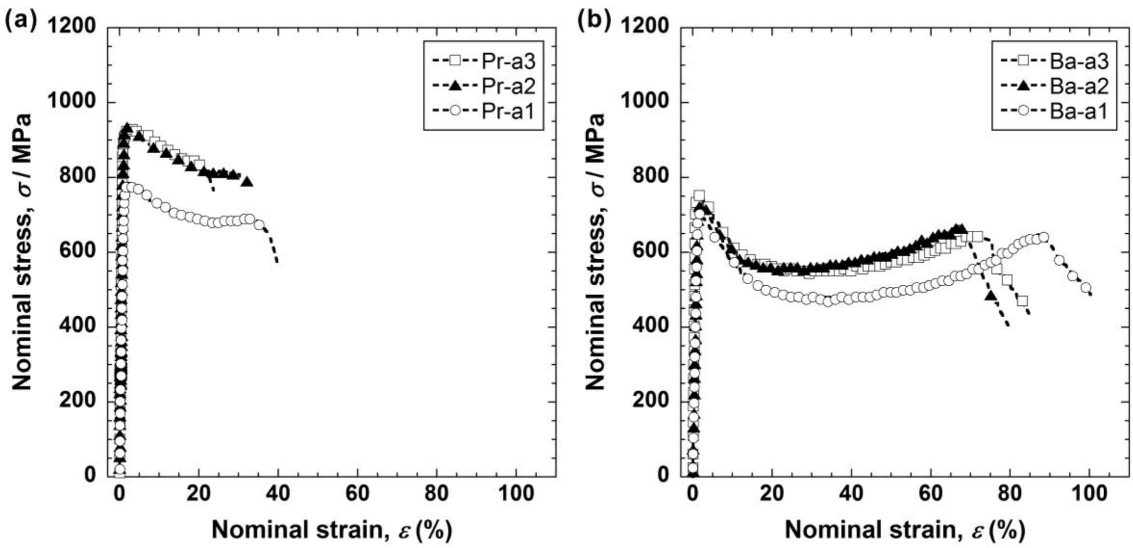

Fig. 3 Stress–strain curves for (a) Pr and (b) Ba specimens.

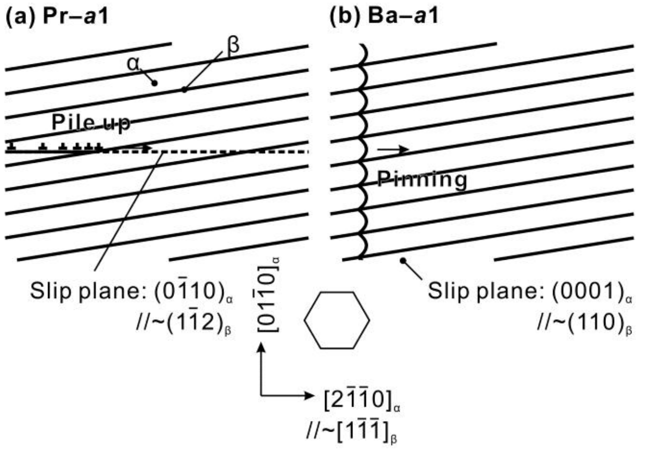

Fig. 4 Schematic illustrations showing different slip blocking morphologies at β laths which intersect with primarily activated slip.

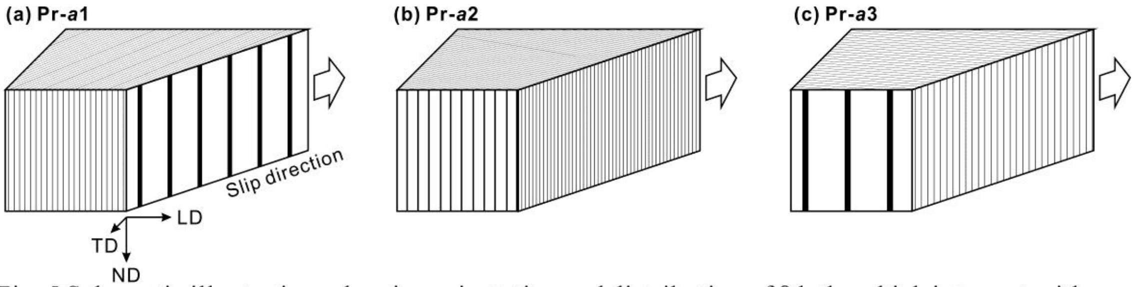

Fig. 5 Schematic illustrations showing orientation and distribution of β laths which intersect with primarily activated slip for Pr specimens.

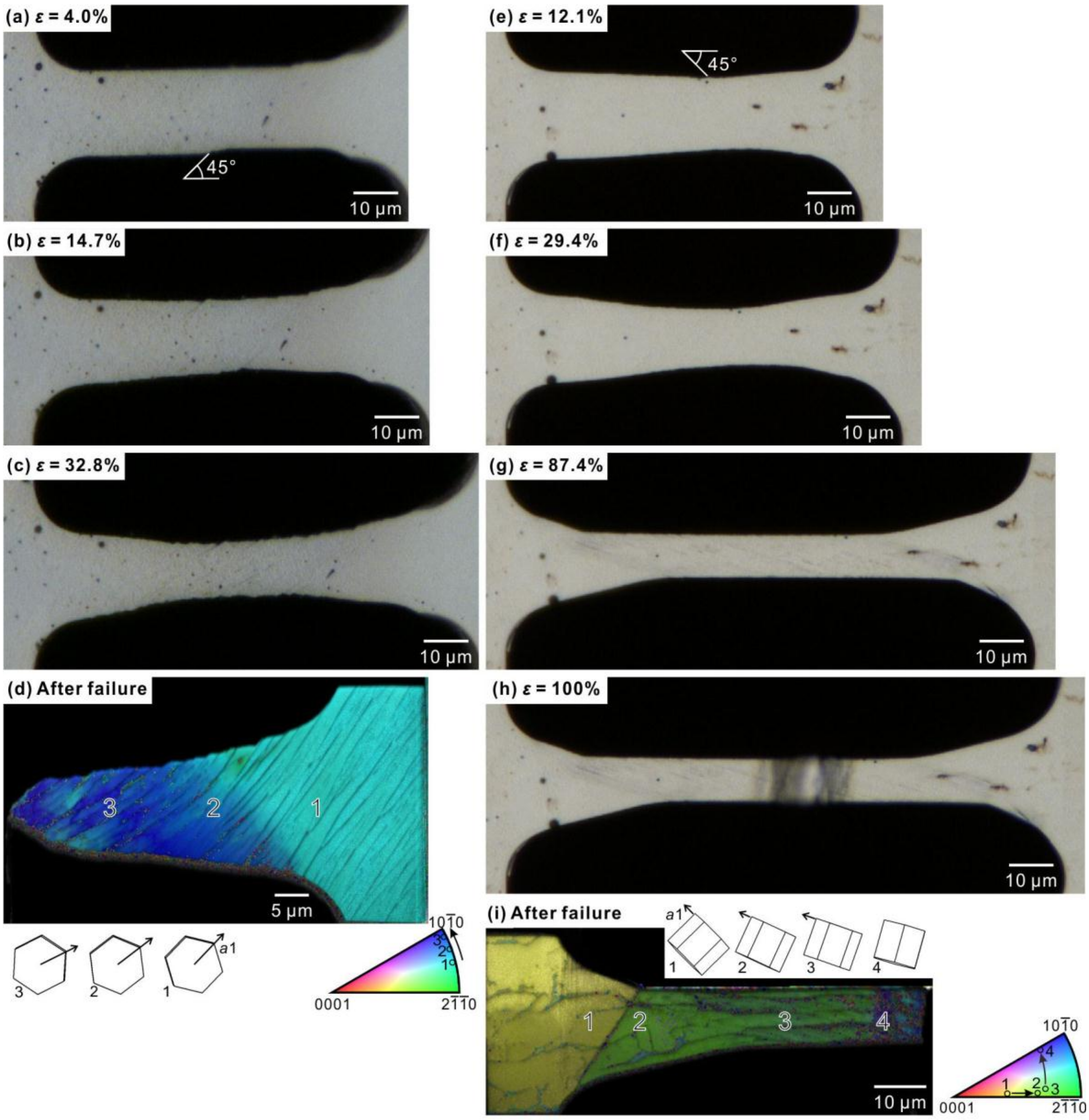

Fig. 6 Optical microscopy images captured during micro-tensile testing and EBSD map colour-coded along the loading direction after failure in (a–d) Pr–$a1$ and (e–i) Ba–$a1$.

Table 1 0.2% proof stress, maximum nominal tensile stress applied, fracture strain, and resolved shear stress (RSS) for yielding.

	0.2% proof stress (MPa)	Maximum nominal tensile stress applied (MPa)	Fracture strain (%)	RSS for yielding (MPa)
Pr-*a*1	753	785	40.0	376
Pr-*a*2	907	934	32.1	453
Pr-*a*3	895	929	23.7	447
Ba-*a*1	684	703	100.3	341
Ba-*a*2	715	729	79.5	357
Ba-*a*3	733	752	85.4	366